frontiers | Frontiers in Materials

ORIGINAL RESEARCH
published: 04 May 2022
doi: 10.3389/fmats.2022.860859

Improved Functionality of Poly(3,4-Ethylenedioxythiophene): Poly(Styrenesulfonate)/ HeptaCoordinated Organotin Complex Films *via* Graphene Applied to Organic Solar Cell Fabrications

María Elena Sánchez Vergara[1]*, *Rafael Imanol Zubillaga Serrano*[1], *Leon Hamui*[1], *José Miguel Galván Hidalgo*[2], *Ismael Cosme*[3] and *Elizabeth Gómez*[2]

[1]Facultad de Ingeniería, Universidad Anáhuac México, Huixquilucan, Mexico, [2]Instituto de Química, Universidad Nacional Autónoma de México, Ciudad de México, Mexico, [3]CONACYT-INAOE, Instituto Nacional de Óptica, Astrofísica y Electrónica (INAOE), Puebla, Mexico

OPEN ACCESS

Edited by:
Jingang Wang,
Liaoning Shihua University, China

Reviewed by:
Xinxi Li,
Guangdong University of Technology, China
Pankaj Madhukar Koinkar,
Tokushima University, Japan

***Correspondence:**
María Elena Sánchez Vergara
elena.sanchez@anahuac.mx

Specialty section:
This article was submitted to Polymeric and Composite Materials, a section of the journal Frontiers in Materials

Received: 23 January 2022
Accepted: 06 April 2022
Published: 04 May 2022

Citation:
Sánchez Vergara ME, Zubillaga Serrano RI, Hamui L, Galván Hidalgo JM, Cosme I and Gómez E (2022) Improved Functionality of Poly(3,4-Ethylenedioxythiophene): Poly(Styrenesulfonate)/ HeptaCoordinated Organotin Complex Films via Graphene Applied to Organic Solar Cell Fabrications. Front. Mater. 9:860859. doi: 10.3389/fmats.2022.860859

Enhanced transparency, conductivity, and stability are some of the most important factors to consider in order to prepare transparent electrodes (TEs) and hole transport layer (HTL) for organic solar cells. In this study, the transparency, optical, and electrical behavior of hybrid films formed by poly(3,4-ethylenedioxythiophene):poly (styrenesulfonate) (PEDOT:PSS) and heptacoordinated organotin (IV) complexes was improved by introducing graphene. The films were deposited by spin-coating and subsequently characterized by infrared and Raman spectroscopy, and by scanning electron microscopy (SEM) and atomic force microscopy (AFM). All the hybrid films transmitted more than 70% of light in the 600–1,000 nm wavelength region, and the optical band gap obtained is in the range of 2.64 and 3.09 eV. In addition, bathophenanthroline (BPhen) was introduced as an electron transport layer (ETL) in order to study the solar cell with complete architecture, conformed by glass/ITO/PEDOT:PSS-graphene-complex/BPhen/Ag. By incorporating the BPhen, the J–V curve current density values were increased, showing a conductivity change of as much as 2.1×10^{-4} S/cm, and under illuminated conditions a more pronounced J–V curve variation (as much as 2.5×10^{1} A/cm^2) was observed. In closing, the devices were subjected to accelerated lighting conditions to determine the stability and operating capacity of the solar cells. The electrical behavior of the devices changed. Within the first 2 h, the electrical behavior improved, where the organotin complex without a substituent (complex-a) device presents higher stability than the complex with the chloride substituent (complex-b) device due to the chloride radical interacting with the BPhen. However, the electrical behavior degraded after 4 h almost eight orders of magnitude in current density due to device films and interface degradation.

Keywords: PEDOT:PSS, graphene, organotin(IV) complex, hybrid film, organic solar cell

INTRODUCTION

Organic semiconductors assume a key part in recent innovative applications because of their fruitful applications in electrical and photovoltaic devices (Alharbi et al., 2016) such as organic solar cells (Günes et al., 2007; Hains et al., 2010), polymer electronic memories (Ling et al., 2008), and thin-film transistors (Vidor et al., 2015). Organic semiconductors are a critical component of devices, and a large variety of π-conjugated molecules and polymers have been used (Ling et al., 2008). Depending on the nature of the charge carriers, the organic semiconductor can function either as a p-type or n-type semiconductor. In p-type semiconductors, the majority carriers are holes, while in n-type semiconductors, the majority carriers are electrons (Ling et al., 2008). Other attractive features of organic semiconductors include good processability of molecular shape and design through chemical synthesis (Raymo, 2002; Ling et al., 2008). In addition, the advantages of organic semiconductors also include simplicity in device structure, good scalability, low-cost potential, low-power operation, multiple state property, and 3D stacking capability (Fu et al., 2004; Yang et al., 2004; Yang et al., 2006; Ling et al., 2008; Dong et al., 2012a). In particular, polymeric materials possess unique properties, such as good mechanical strength, flexibility, and ease of processing (Ling et al., 2008; Dong et al., 2012a). It is important to consider that as alternatives to the more elaborated vacuum evaporation processes, solution processes, including spin-coating, can be used to deposit polymers onto a variety of substrates such as plastics (e.g., polyethylene terephthalate), silicon wafers, glass, quartz, and conductive electrodes (e.g., Al, Ag, and indium tin oxide) (Ling et al., 2008; Dong et al., 2012a).

As one of the most well-known conjugate polymers, PEDOT:PSS (poly(3,4-ethylene dioxythiophene)–polystyrene sulfonic acid), a mixture of two polymers, has proved its value in the development of several electronic devices. PSS is a surfactant polymer that has two functions: the first one is to balance the charge of the PEDOT molecule (Jonas and Heywang, 1994) and the second one is to act as a dispersant of PEDOT in water (De Kok et al., 2004). The PEDOT:PSS (**Figure 1**) presents excellent functionalities in optoelectronics due to the fact that highly transparent thin films, in their doped state, conductors, and electrochemically stable can be obtained. Recently, the combination of conductive PEDOT:PSS with another type of structures that are chemically different such as transition metal dichalcogenide (TMD) nanosheets (Sajedi-Moghaddam et al., 2017) or carbon-based materials (Kepić et al., 2014; Sarkhan et al., 2019) has received increasing attention not only for the improvement of the electrical properties of these hybrid nanostructures but also for their use in various types of electronic applications. Carbon-based materials, such as graphene, are good candidates for fabricating hybrid films with PEDOT:PSS through surface modification and stabilizing techniques (Yoo et al., 2014). Because of their π–π stacking interactions, the conjugated aromatic chains of PEDOT:PSS can be stably fixed on graphene sheets without destroying the electronic structure of graphene (Kepić et al., 2014). The electrical conductivity of PEDOT:PSS is not high enough for high-performance applications, which results in electronic packaging with poor efficiency and reliability (Chen et al., 2016). However, the electrical properties of PEDOT:PSS can be improved by graphene doping (Kim et al., 2012; Yoo et al., 2014; Chen et al., 2016; Hilal and Han, 2018). Graphene has excellent electrical properties since it is an allotrope of carbon

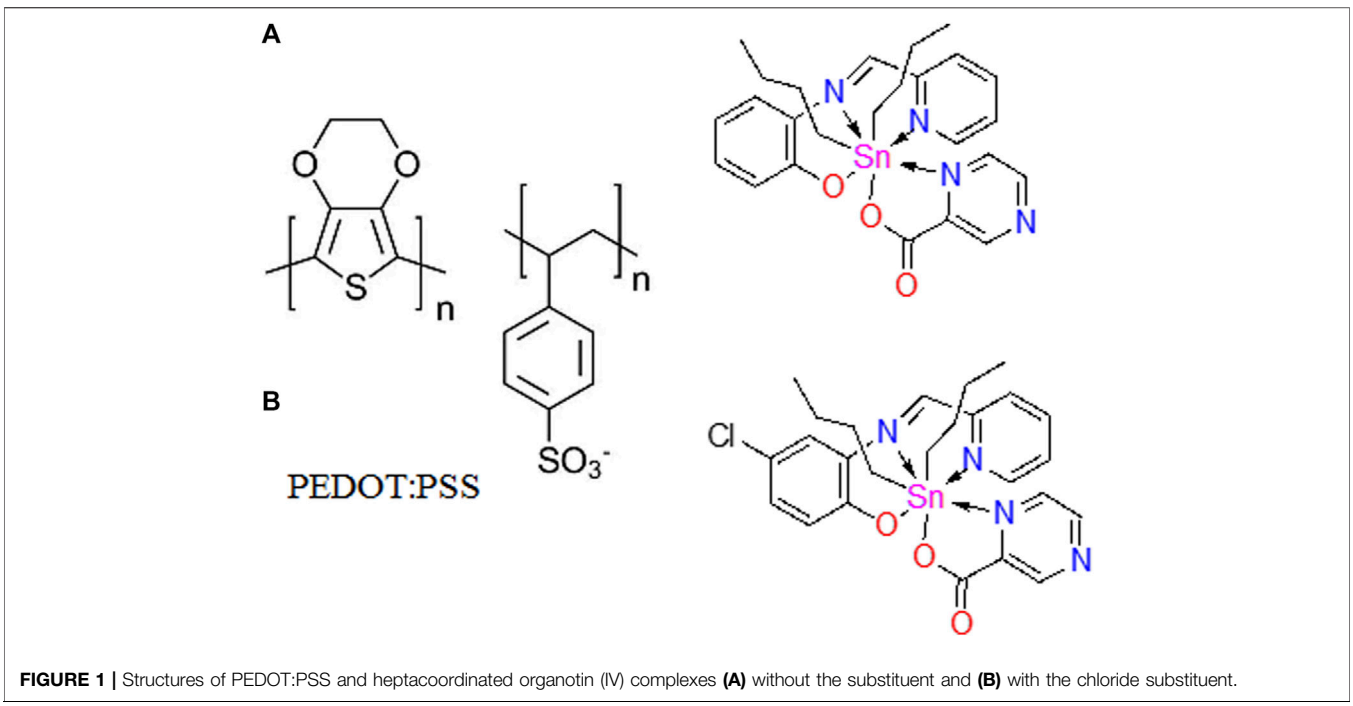

FIGURE 1 | Structures of PEDOT:PSS and heptacoordinated organotin (IV) complexes **(A)** without the substituent and **(B)** with the chloride substituent.

with a single two-dimensional (2-D) layer of sp^2-hybridized carbon atoms. This layer of carbon atoms has attracted interest with regard to electronic applications because of its superior charge mobility and mechanical strength (Kim et al., 2012; Kepić et al., 2014). PEDOT:PSS mixed with graphene as a functioning material has been set up for application in gas thin-film sensors (Oh et al., 2020). The 2-D structure of graphene has a higher sensing territory for every unit of volume and less noise than other solid-state sensors (Oh et al., 2020). The π–π stacking interactions between graphene and the polymer result in an enhanced electrical conductivity, chemical stability, and thermoelectric performance (Park et al., 2017).

In addition, heptacoordinated organotin (IV) complexes (see **Figure 1**) were added to the films PEDOT:PSS-graphene in order to manufacture films that serve as active layers in optoelectronic devices. The heptacoordinated organotin (IV) complexes used are small molecules with different substituents that can increase the efficiency in the devices (Sánchez Vergara et al., 2021). Some authors of the current work have studied this type of tin complexes and their application in optoelectronic devices (Sánchez Vergara et al., 2020; Monzón-González et al., 2021; Sánchez Vergara et al., 2021). It has been found that their presence in thin films promotes the electric charge transport due to their structure π-conjugated structure and also due to the presence of electronegative atoms and of substituents coordinated to the metal. These types of complexes give rise to a variety of structures that can usually be modulated by changing the substituents bonded to the tin atom, such as the construction of well-organized supramolecular architectures supported by strong metal–ligand coordination bonds (Gholivand et al., 2015). Organotin complexes are widely known by their potential as PVC stabilizers (Ghazi et al., 2018; Mahmood et al., 2020; Ahmed et al., 2021); however, their potential applications in organic solar cells have been scarcely explored (Cantón-Díaz et al., 2018). Based on the abovementioned facts, our aim in this work is to manufacture photovoltaic devices with conventional bulk heterojunction (BHJ) architecture using highly efficient hybrid PEDOT:PSS-graphene-organotin complex films. The function of the polymer and graphene was as a hole transport layer (HTL) and transparent electrode (TE), while the function of the tin complexes was as components of the active layer of the device. The novelty of the work is related to using hybrid films with BHJ conformation with carbon-based materials such as graphene with PEDOT:PSS to generate HTL and TE in the device and finally to increase the efficiency of the devices by means of an electron transport layer (ETL) of bathophenanthroline (BPhen). The films were morphologically and structurally characterized; in addition, the optical behavior was evaluated through the obtention of parameters such as transmittance, absorption coefficient, and band gap. The photovoltaic devices were evaluated in their electric and photovoltaic behavior under different radiation and temperature conditions. Finally, the devices were subjected to accelerated irradiation conditions to determine the stability of the films and operating capacity of the photovoltaic device.

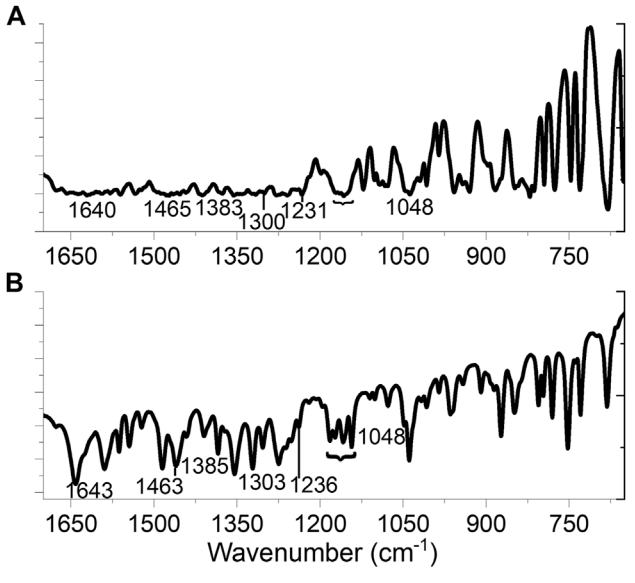

FIGURE 2 | IR spectrum of PEDOT:PSS-graphene-organotin complex films. **(A)** Organotin complex without the substituent and **(B)** with the chloride substituent.

TABLE 1 | Spin-coater operating parameters.

STEP	Spin speed (rpm)	Spin time (s)	Acceleration (rpm/s^2)
1	200	11.00	40.00
2	1,400	8.00	200.00
3	0	7.00	200.00

MATERIALS AND METHODS

All reagents and solvents were obtained from commercial suppliers (Sigma-Aldrich) and used without further purification. The heptacoordinated tin (IV) complexes were obtained according to methods previously reported by some of the authors of the present work (Sánchez Vergara et al., 2021). The hybrid films were deposited by the spin-coating technique, and a Smart Coater 200 equipment was used. The dispersion used for the manufacture of the films consisted of 6 ml of graphene-PEDOT:PSS hybrid dispersion in dimethylformamide (Sigma-Aldrich). Subsequently, a saturated dispersion was generated with the tin compound without the substituent (complex **a**) and with the chloride substituent (complex **b**) (see **Figure 1**). The mixture graphene-PEDOT:PSS-organotin (IV) complex was dispersed using the G560 shaker of Scientific Industries Vortex-Genie. The dispersion was later deposited on the substrate, and the equipment was operated with the parameters shown in **Table 1**.

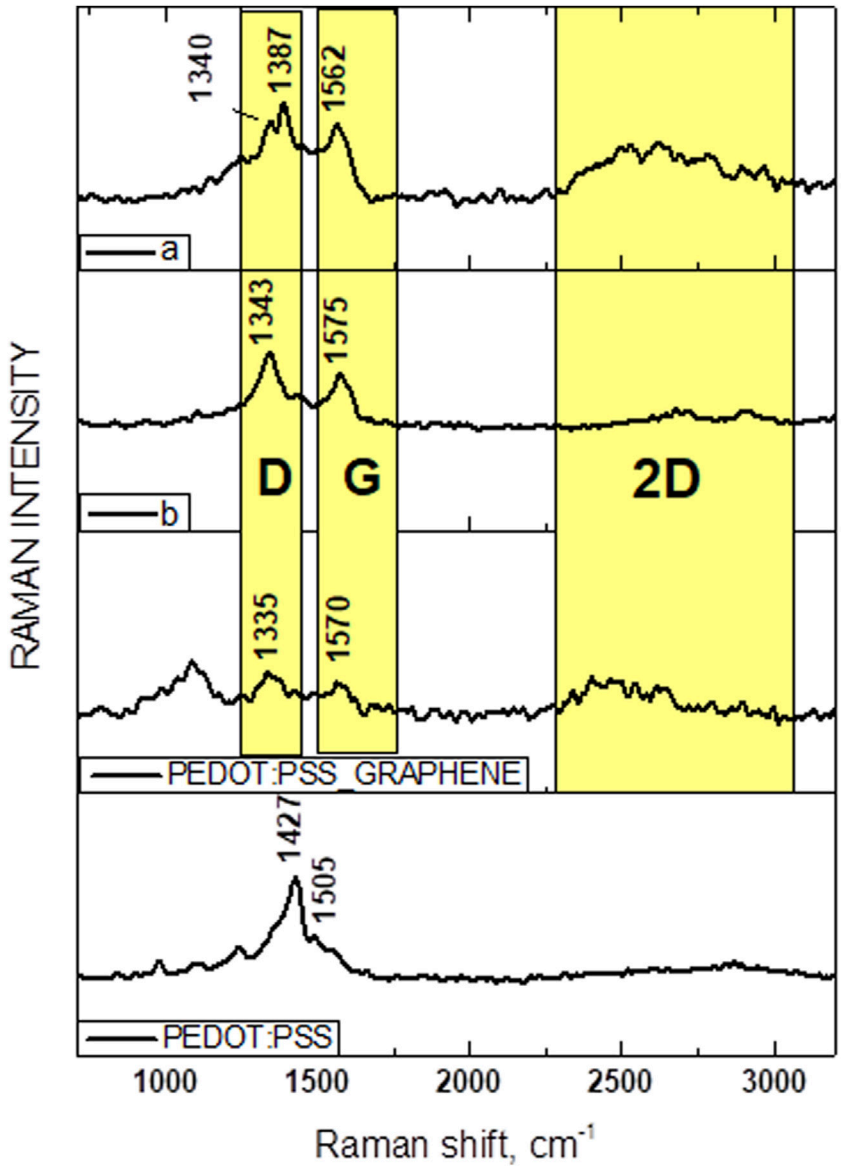

FIGURE 3 | Raman spectra of the PEDOT:PSS film without graphene, PEDOT:PSS-graphene, PEDOT:PSS-graphene-**a** complex, and PEDOT:PSS-graphene-**b** complex films.

While accelerating, in step 1, 0.1 ml of the graphene/PEDOT:PSS mixture was deposited on the substrate, followed by 0.15 ml in step 2. After completing step 3, the substrate was then removed from the spin-coating machine and left to dry at room temperature. Once the substrate was visibly dry, it was placed back in the spin-coating machine. This process was repeated seven times followed by drying at 80°C for 3 min and the thin films were deposited in monocrystalline n-type silicon wafers (c-Si), corning glass, and glass coated with indium tin-oxide (In_2O_3/SnO_2; ITO) substrates. The corning glass and the ITO glass substrates were at first sequentially washed in an ultrasonic bath with dichloromethane, methanol, and acetone. The silicon substrate was washed with a "p" solution (10 ml HF, 15 ml HNO_3, and 300 ml H_2O) to remove surface oxide. FT-IR spectroscopy analysis was performed for the compounds as KBr pellets and for the films on the silicon substrate using a Nicolet iS5-FT spectrometer at a wavelength range of 4,000–500 cm^{-1}. Raman spectra were measured in films on the glass substrate with an AFM-Raman of Ntegra Spectra Systems with an excitation laser wavelength of 532 nm. Topographic and morphological characteristics were investigated with an atomic force microscope (AFM) using an Ntegra platform and with a ZEISS EVO LS 10 scanning electron microscope (SEM) for the films deposited on the glass substrate. The absorbance and transmittance of the films on glass were obtained in the 200–1,100 nm wavelength range on a UV–Vis

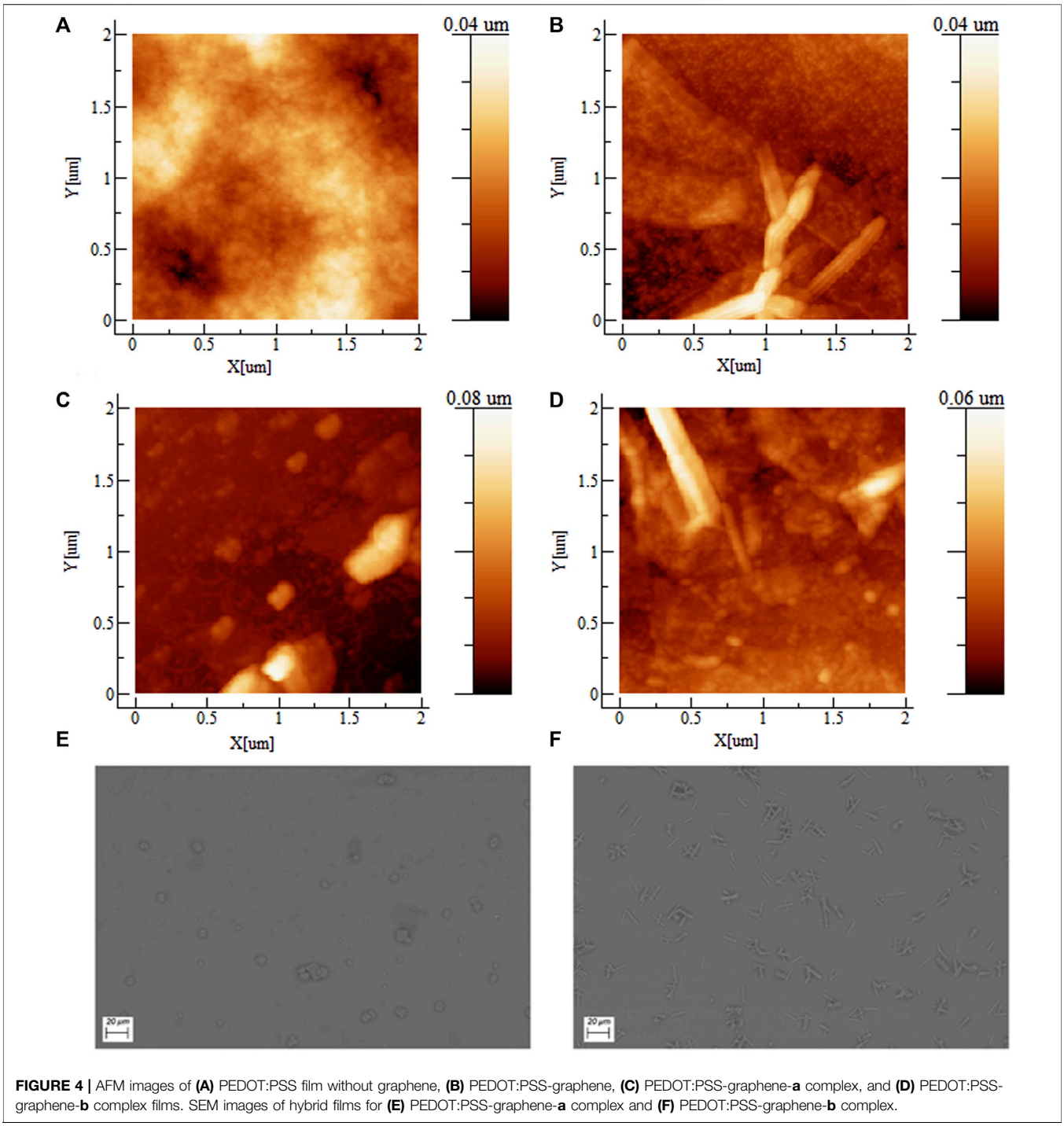

FIGURE 4 | AFM images of **(A)** PEDOT:PSS film without graphene, **(B)** PEDOT:PSS-graphene, **(C)** PEDOT:PSS-graphene-**a** complex, and **(D)** PEDOT:PSS-graphene-**b** complex films. SEM images of hybrid films for **(E)** PEDOT:PSS-graphene-**a** complex and **(F)** PEDOT:PSS-graphene-**b** complex.

300 Unicam spectrophotometer. For the electrical characterization of the films, organic solar cells were fabricated using ITO as the anode and silver as the cathode. For this evaluation, a programable voltage source, a sensing station with lighting and temperature controller circuit from Next Robotix, and an auto-ranging Keithley 4200-SCS-PK1 pico-ammeter were used. Finally, in order to increase the efficiency in the device mentioned above, the BPhen films were deposited using a high-vacuum thermal evaporation system using molybdenum crucibles. The BPhen was heated to 570 K, sublimated at a vacuum pressure of 5×10^{-6} Torr, and the deposit speed was 11.4 Å/s. The thickness of each film was monitored using a microbalance quartz crystal monitor, connected to a thickness sensor. The external quantum efficiency (EQE) in the device was obtained using a QUESA-1200 system with an LED light source.

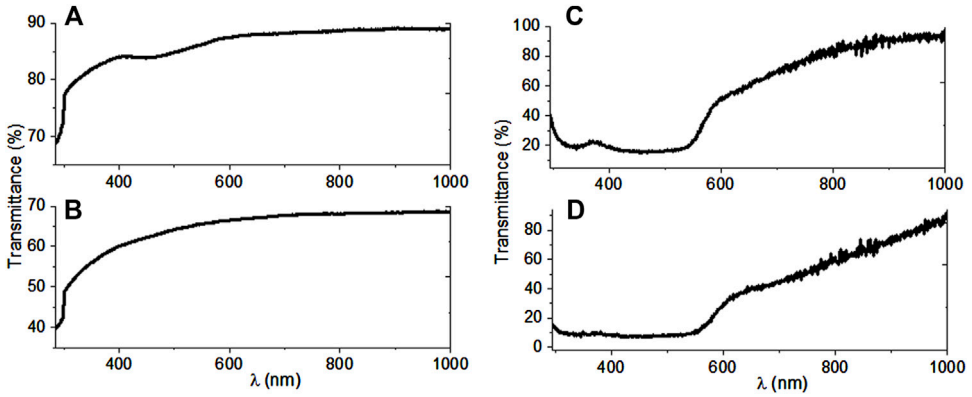

FIGURE 5 | Transmittance spectra of **(A)** PEDOT:PSS-graphene-**a** complex, **(B)** PEDOT:PSS-graphene-**b** complex, **(C)** PEDOT:PSS-**a** complex, and **(D)** PEDOT:PSS-**b** complex films.

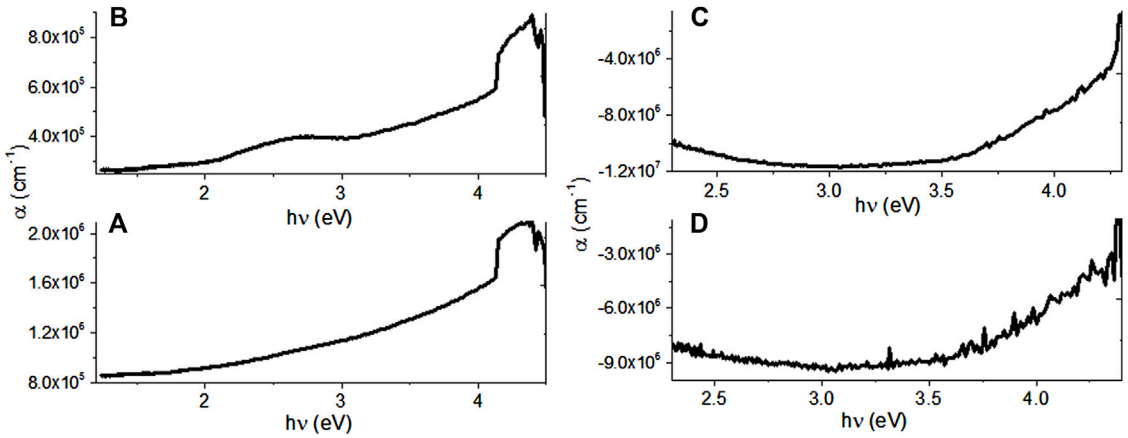

FIGURE 6 | Variation of α with $h\nu$ for **(A)** PEDOT:PSS-graphene-**a** complex, **(B)** PEDOT:PSS-graphene-**b** complex, **(C)** PEDOT:PSS-**a** complex, and **(D)** PEDOT:PSS-**b** complex films.

RESULTS AND DISCUSSION

Characterization of Hybrid Films

After depositing the PEDOT:PSS-graphene-organotin hybrid films by spin-coating, the presence and stability of the heptacoordinated organotin (IV) complexes should be verified by IR spectroscopy. The spectra for the two hybrid films are shown in **Figure 2**: 1) the vibration bands ν(C = N) at 1,584 ± 5 cm^{-1}, 2) the appearance of the vibration band ν(C–O) between 1,145 ± 2 and 1,163 ± 3 cm^{-1}, and 3) the two vibrational bands with two different absorptions in the range of 1,351 ± 3 cm^{-1}–1,641 ± 1 cm^{-1}, which correspond to the symmetric ν_{sym} (COO) and asymmetric ν_{asym} (COO) stretching vibrational modes of the carboxyl group (Sánchez Vergara et al., 2021). These results give an indication of the feasibility to manufacture hybrid films with the heptacoordinated organotin (IV) complexes. Apparently, these complexes were embedded in the polymer–graphene matrix and did not suffer chemical decomposition during their deposit. With respect to PEDOT:PSS and graphene in the spectra of **Figure 2**, their signals are shown and, in addition, from them, sufficient binding and chemical interactions are observed (Rattana et al., 2012; Yoo et al., 2014). Visible signals in the range of 682 and 950 cm^{-1} are assigned to aromatic sp2 and out-plane C–H bending in the polymeric chain or marginally C–O stretches at graphene planes (Rattana et al., 2012; Yoo et al., 2014). The multipeak reflection at 1,140–1,185 cm^{-1} indicates C–O–C bindings on the graphene surface (Yoo et al., 2014). The two absorption peaks at 1,233 ± 3 and 1,048 cm^{-1} are assigned to the C–O stretching vibrations, and the signals at 1,301 ± 2 cm^{-1} show the C–O stretches originated from weak C-O···H electrostatic bands which occur due to the interaction between unsaturated C-groups at graphene. This kind of binding is responsible for the stable dispersion of graphene in the PEDOT:PSS matrix by making bridges between graphene and sulfur groups at the PSS segments of PEDOT:PSS (Yoo et al., 2014; Soltani-kordshuli et al., 2016). The multiple peaks found

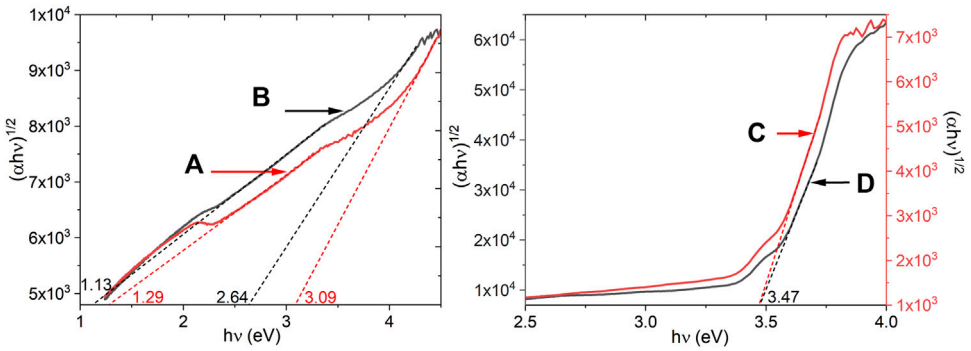

FIGURE 7 | Variation of $(\alpha h\nu)^{1/2}$ with $h\nu$ for **(A)** PEDOT:PSS-graphene-**a** complex, **(B)** PEDOT:PSS-graphene-**b** complex, **(C)** PEDOT:PSS-graphene-**a**-BPhen, and **(D)** PEDOT:PSS-graphene-**b**-BPhen films.

around 1,384 ± 1 cm^{-1} are attributed to the C–O bond in PEDOT, and the last two peaks at 1,464 ± 1 and 1,642 ± 2 cm^{-1} reflect C = C group stretches in PSS (Rattana et al., 2012; Yoo et al., 2014; Soltani-kordshuli et al., 2016). According to Pasha et al. (2019), the IR spectra substantiate that the graphene was well-dispersed in the PEDOT:PSS and that the tin complex is also embedded and scattered in the polymer matrix.

Raman spectroscopy, shown in **Figure 3**, was performed to complement the results obtained by IR spectroscopy. From the main bands in the Raman spectrum, it is possible to detect the benzoid structure of PEDOT in the film (Ouyang et al., 2005; Yeon et al., 2017). The main bands in the Raman spectrum of the PEDOT:PSS film are assigned to the symmetric (1,425–1,434 cm^{-1}) and asymmetric (1,503–1,509 cm^{-1}) C=C stretching vibrations. The Raman spectrum in **Figure 3** for the PEDOT:PSS-graphene sample shows a change of the main bands of PEDOT:PSS in intensity and positions with the presence of the characteristic D, G, and 2D bands of graphene, indicating that this is incorporated into the PEDOT:PSS matrix. The D band corresponds to vibrations of dangling bonds of carbon atoms, while the G band corresponds to the vibration of sp2-bonded carbon atoms (Du et al., 2018). The 2D band sensitively depends on the symmetry properties and number of graphene layers (Malard et al., 2009). The samples PEDOT:PSS-graphene-**a** complex and PEDOT:PSS-graphene-**b** complex show broadening and shift of the D and G bands, indicating changes in the electronic structure of graphene in the presence of electron-acceptor groups (Luceño Sánchez et al., 2018). In addition, changes in the 2D band in these samples suggest changes in the number of ayers and structure of graphene, supporting the observation in AFM results (see **Figure 4**). These results demonstrate a strong π–π interaction between the PEDOT:PSS layer and graphene that can result in the changes of charge carrier mobility of PEDOT:PSS films.

In order to determine the topography and morphology in the hybrid films, AFM and SEM were performed. The AFM images of the morphology surface in a 2 × 2 μm area for 1) PEDOT:PSS film without graphene, 2) PEDOT:PSS-graphene, 3) PEDOT:PSS-graphene-**a** complex, and 4) PEDOT:PSS-graphene-**b** complex films are shown in **Figure 4**. The AFM images confirm the presence of bended graphene in the surface of the PEDOT:PSS layer. In accordance with literature data (Yoo et al., 2014; Pasha et al., 2019), the pure PEDOT:PSS film in **Figure 4A** had a smooth surface. The samples PEDOT:PSS-graphene (see **Figure 4B**) and PEDOT:PSS-graphene-**b** complex (**Figure 4D**) show elongated needle-type structures that are not in the PEDOT:PSS film without graphene. It is interesting to note that these structures show a 3D thin graphene skeleton as is reported by Dong et al. (2012b). On the other hand, the film PEDOT:PSS-graphene-**a** complex (**Figure 4B**) shows the presence of sheet structures more characteristic of graphene raw materials (Chen et al., 2016; Lovén et al., 2021). Considering that all films were deposited under the same concentration, equipment operation, and substrate conditions, the different shape in the graphene is due to the type of the tin complex used. Apparently, the complex-**a** inhibits the preferential growth directions in graphene. In **Figures 4E,F**, the microphotographs at 750x of the films PEDOT:PSS-graphene-organotin complex are shown. The SEM images demonstrate a considerable coverage of the polymer on the graphene and tin complexes, and the continuity of the films is a good approximation to improve the transport of charge and its mobility, which can be reflected in the optical properties of the films.

The spectra of transmittance, T(λ), in the wavelength range 275–1,000 nm for the two hybrid films are depicted in **Figures 5A,B**. The results demonstrate that all the hybrid films transmitted more than 70% of light in the wavelength region of 580–1,000 nm, but the transmittance is considerably higher in the films of the PEDOT:PSS-graphene-**a** complex. This result can be justified by the graphene morphology and by a higher conjugation in the **a**-complex molecule and by a lower polarity in it. In the spectral region where λ> 580 nm, the films are highly transparent and the films are non-absorbing (Alharbi et al., 2016; Al-Muntaser et al., 2018; Makhlouf et al., 2019). On the other hand, in **Figures 5C,D**, the spectrum for the films PEDOT:PSS-organotin complex without graphene is observed. The change in transmittance with respect to the films with graphene is significant. Two zones were observed for these spectra: the first region corresponds to a shorter wavelength range at $\lambda <$ 580 nm. This region exhibits absorption, which is called the

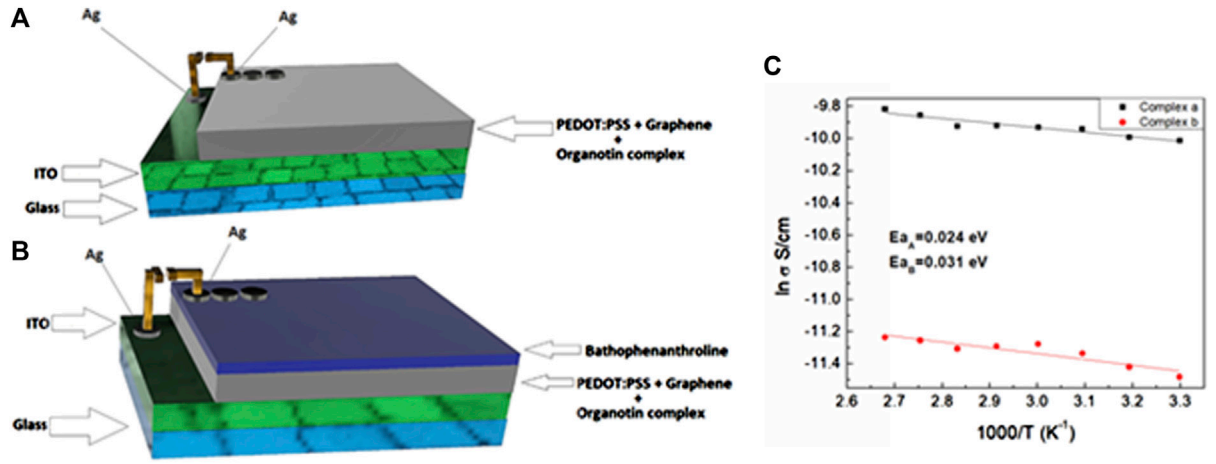

FIGURE 8 | Device structure for **(A)** PEDOT:PSS-graphene-complex and **(B)** PEDOT:PSS-graphene-complex/BPhen. **(C)** Electrical conductivity Arrhenius plot for PEDOT:PSS-graphene-a and PEDOT:PSS-graphene-b devices.

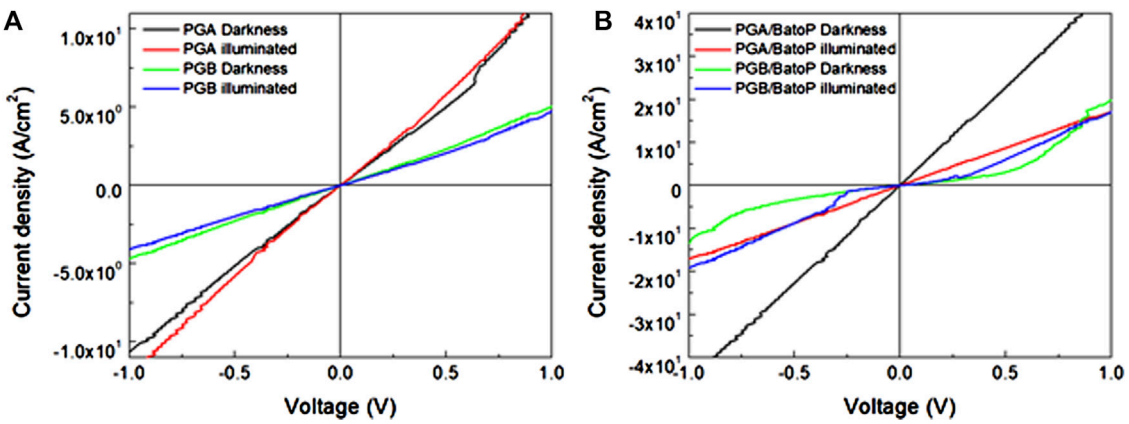

FIGURE 9 | Darkness and illumination condition J–V curves for **(A)** PEDOT:PSS-graphene-a and PEDOT:PSS-graphene-b devices, and **(B)** with BPhen.

UV–Vis absorption region of the films (Makhlouf et al., 2019). As for the second region, which encompasses a larger wavelength of λ> 580 nm, it is known as the infrared non-absorbing region, which reveals that the films were clear, and no light is absorbed (Makhlouf et al., 2019). The presence of graphene significantly increases the transmittance in the violet-to-blue range of the electromagnetic spectrum (300–580 nm). These results are important because they are opposite with those obtained by Chen et al. (2016) for films with PEDOT:PSS and graphene fabricated by ultrasonic vibration–assisted substrate spray coating and by Kepic et al. (Kepić et al., 2014) for PEDOT:PSS films doped with graphene quantum dots. In this work, the presence of the heptacoordinated organotin (IV) complexes favors the high transmittance of the films with graphene. In addition, the transparency level of the PEDOT:PSS-graphene-complex films is in accordance with literature data (Seol et al., 2012; Kepić et al., 2014; Lee et al., 2014; Chen et al., 2016; Hilal and Han, 2018). Due to the good optical transparency of the films, they would be an effective option to use as a transparent electrode or HTLs in the field of photonics and organic electronics (Kepić et al., 2014; Lee et al., 2014; Chen et al., 2016; Hilal and Han, 2018). The films without graphene would have similar application, but at wavelengths greater to 580 nm, which limits their performance in this type of devices.

In addition, the transmittance (T) was used to calculate the absorption coefficient (α) through the equation: $\alpha = \ln(T/d)$, where d is the thickness of the films. In this process, the energy of the photon $h\nu$ was obtained from the inverse of the wavelength (λ), the speed of light (c), and of Planck's constant (h): $h\nu = hc/\lambda$. **Figure 6** shows the variation of the α, with $h\nu$ for films with graphene (**Figures 6A,B**) and without graphene (**Figures 6C,D**). For the case of the films without graphene, a very low absorption coefficient is presented, which is an indication of the important effect that graphene exerts on the optical properties of the heptacoordinated organotin (IV) complexes. **Figure 6A** shows that the value of the α is in the order of 10^{-5} cm^{-1} for

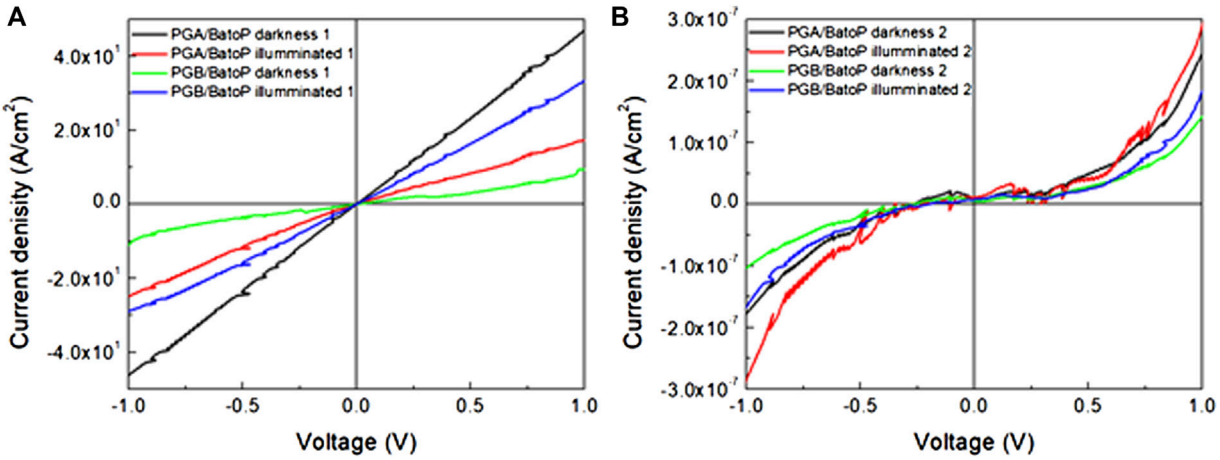

FIGURE 10 | Darkness and illumination condition J–V curves for PEDOT:PSS-graphene-a/BPhen and PEDOT:PSS-graphene-b/BPhen devices, after a **(A)** 2 h and **(B)** 4 h light exposition.

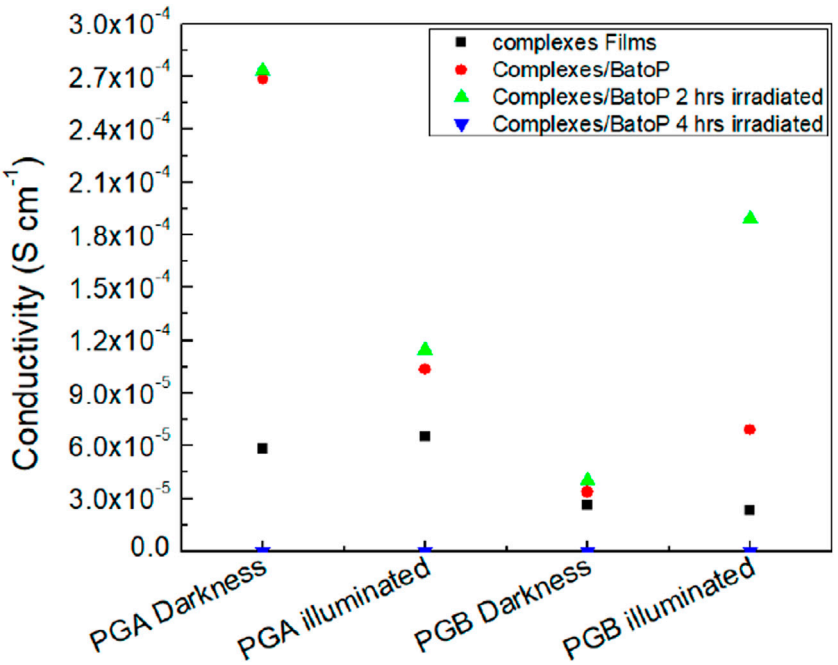

FIGURE 11 | Comparison chart of the darkness and illumination conductivity for **(A)** PEDOT:PSS-graphene-**a** and **(B)** PEDOT:PSS-graphene-**b** devices, after adding BPhen and irradiating for 2 and 4 h.

the film with complex-**a,** and **Figure 6B** shows that the value of α is 10^{-6} cm^{-1} for the film with complex-**b**. In addition, for the PEDOT:PSS-graphene-**a** complex film, the high Soret band is observed at 2.7 eV. The peak of the Soret band is generally interpreted by the excitation between the bonding and antibonding molecular orbital in terms of π–π* (Alharbi et al., 2016; Ouyang et al., 2005; Yeon et al., 2017; El-Nahass et al., 2011a; Pal et al., 1993; El-Nahass et al., 2011b). Apparently, the π-conjugated structure of complex-**a** and the morphology of graphene are responsible for discrete transitions beyond the Soret band (Alharbi et al., 2016; Cotter et al., 1999). Finally, in **Figures 6A,B**, the π–π* transition peak at 4.3 eV can be observed, same place in which a shoulder peak is located and one can observe a shoulder in this place, which is originated from π–π* transition of the C = C bond of graphene (Dong et al., 2012c; Zhang et al., 2012; Kepić et al., 2014).

It is important to consider that the optical bandgap (E_g^{opt}) in organic semiconductors is directly related to its π-conjugated system. There is a procedure that relates α to the E_g^{opt} associated with the films and is carried out by extrapolating the linear trend

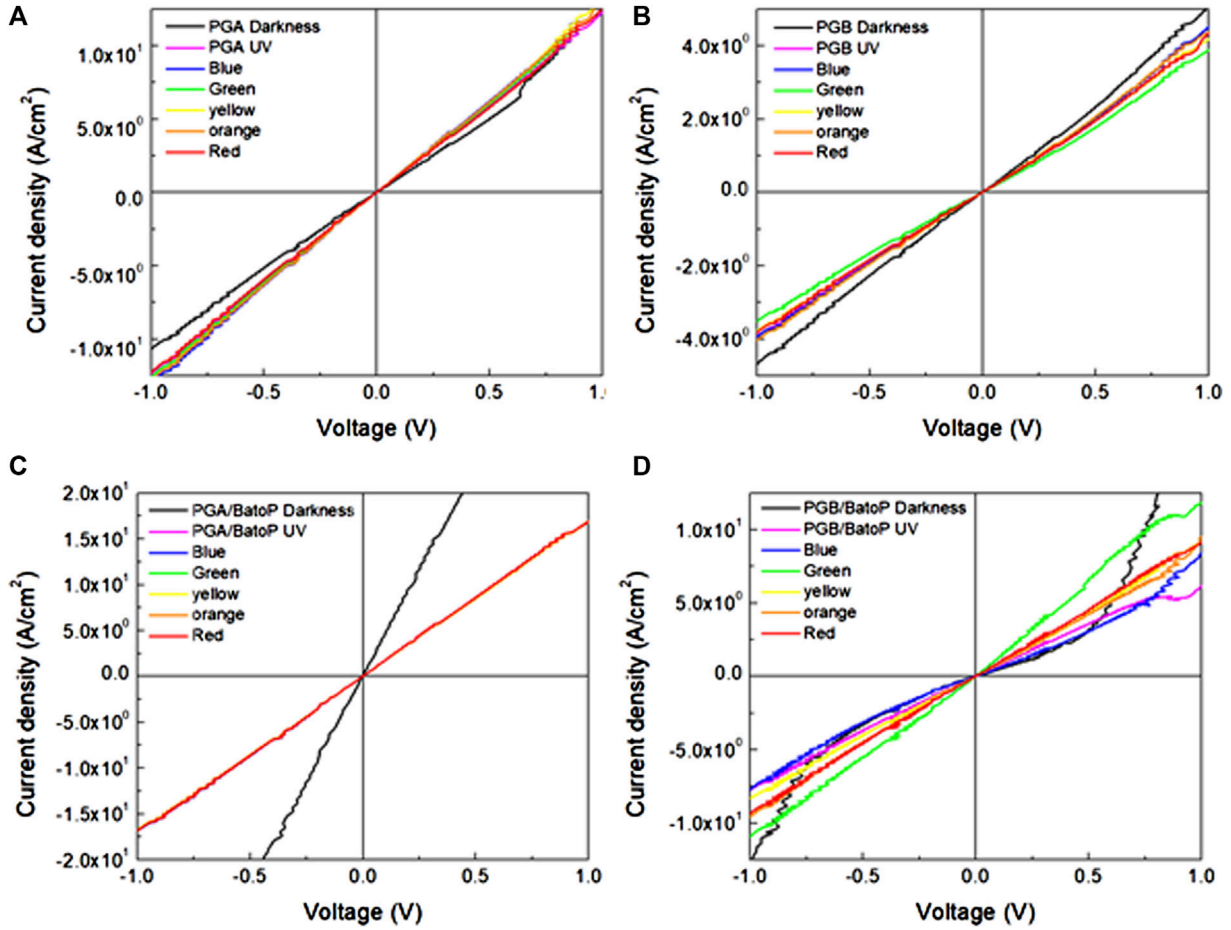

FIGURE 12 | Different light color exposure J–V curves for **(A)** PEDOT:PSS-graphene-a, **(B)** PEDOT:PSS-graphene-b, **(C)** PEDOT:PSS-graphene-a/BPhen, and **(D)** PEDOT:PSS-graphene-b/BPhen devices.

observed in the spectral dependence of $(\alpha h\nu)^{1/2}$ over $h\nu$ (Laidani et al., 2008; Kamiya et al., 2009; Urbach, 1953; Mok and O'Leary, 2007; Tsiper et al., 2002). The graph of $(\alpha h\nu)^{1/2}$ vs. $h\nu$ is shown in **Figure 7**, and the E_g^{opt} is evaluated from the *x*-axis that intercepts at $(\alpha h\nu)^{1/2} = 0$. For the PEDOT:PSS-graphene-organotin complex films, the values are recorded in **Figure 7** and correspond to the onset of optical absorption and formation of a bound electron-hole pair or exciton "Frenkel exciton" (Zhokhavets et al., 2003; El-Nahass et al., 2011a) and the fundamental energy gap (Zhokhavets et al., 2003; El-Nahass et al., 2011a). The values obtained are lower for the film with the complex-**b**, which can be attributed to the effect of the chlorine atom and the elongated needle-type structure for graphene. However, in both hybrid films, the band gap obtained places these materials within the range of organic semiconductors. Although for its use in optoelectronic devices, it is important to establish the function of each component within the hybrid film and enhance its operation in the device, adding interfacial films that promote an efficient charge transport. The function of the PEDOT:PSS and graphene is as an HTL and TE, and the function of the tin complexes was as components of the active layer of the device and to increase the efficiency of the devices. BPhen was introduced in the PEDOT:PSS-graphene-organotin complex system, such as ETL. The presence of this ETL layer affects in such an important way the E_g^{opt}. In **Figures 7C,D** are observed the curves $(\alpha h\nu)^{1/2}$ vs. $h\nu$ and the fundamental gap for these systems. The presence of the Bphen increases the fundamental gap to 3.47 eV; however, the curves for both films align to the same behavior.

Device Fabrication and Electrical Characterization

For electrical characterization, two different device structures were fabricated. These structures are shown in **Figures 8A,B**. The first device structure is constituted by glass/ITO/PEDOT:PSS-graphene-complex/Ag and the second by glass/ITO/PEDOT:PSS-graphene-complex/BPhen/Ag. The films were studied by varying the temperature, where an increase of conductivity is expected. The conductivity has the general form:

$$\sigma = \sigma_0 \exp\left(-\frac{E_a}{kT}\right),$$

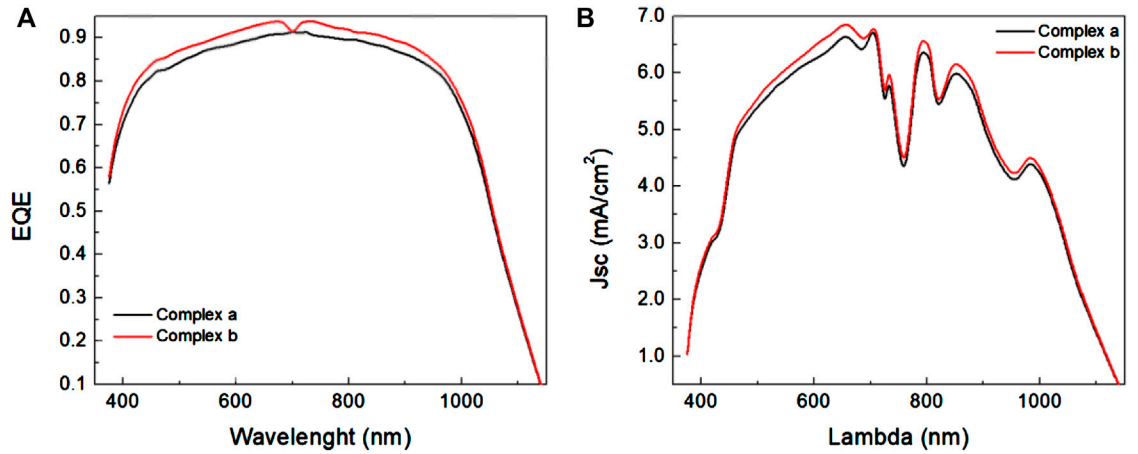

FIGURE 13 | PEDOT:PSS-graphene-a and PEDOT:PSS-graphene-b devices **(A)** EQE and **(B)** J_{sc}.

where E_a is the thermal activation energy of the electrical conductivity, σ_0 is the pre-exponential factor depending on the material nature, and k is Boltzmann's constant (1.38×10^{-23} J/K). **Figure 8C** shows the Arrhenius plot for the graphene compounds, where it is observed that the conductivity of both films increases with the temperature, and there is a variation in the slope comparing both devices. From these slopes, the activation energy was calculated and is of 0.024 eV for complex-**a** while is of 0.031 eV for complex-**b**. These values are close to the E_a of the PEDOT:PSS (Gueye et al., 2016; Akbari et al., 2018; Mansour et al., 2020). The latter indicates that the lower thermal activation energy E_a for complex-**a** is due to its greater capacity to receive electrons, an inferred reduction of the energy between the conduction band and the donor level. In addition, the conductivities obtained for complex-**a** are higher than those for complex-**b** and may be related to the graphene shape that favors the transport of electric charges.

Figure 9 shows the J–V curves for darkness and illumination conditions of the PEDOT:PSS-graphene-a and the PEDOT:PSS-graphene-b devices and also the devices that include the BPhen. All of the curves in **Figure 9A** present an apparent linear behavior, and the characteristic current density is larger for the a-device. It is observed that for both complexes, the curve for illuminated conditions varies with respect to the darkness conditions, indicating a photo-response of the devices. For the a-device, the illuminated curve shows larger current density values than the darkness curve, but for b-device, the opposite is observed, which may be related to a higher charge carrier recombination rate due to traps. However, this variation is more pronounced for a-device that may be related to the resulting larger absorption coefficient. On the other hand, devices with BPhen J-V curves are shown in **Figure 9B**, where the current density values are larger for the a-device. A change in the curve shape is observed for the b-device that can be related to the large particle size in the graphene observed previously. The current density values are larger than those of the devices without the BPhen (**Figure 9A**) related to the morphological change and the improved charge transport consequence of the BPhen addition. In addition, it can be observed that the illumination effect on the J–V curves is larger than that shown in **Figure 9A**. However, by comparing **Figure 9B** curves, this effect is more pronounced for a-device such that besides the absorption changes due to the particle shape, size, and distribution of complex-a, it allows a larger photon absorption and therefore charge carrier generation. Nevertheless, for the a-device illuminated curve, smaller current density values than those of the darkness curve are shown, but for b-device, the opposite is observed. Despite the current density increase due to the BPhen, under operation of the solar cell, a reduction of the charge carrier collection may be due to an increase of the trapping sites within the hybrid films, the BPhen, and due to the interfaces. In addition, a change in curve shape is observed for b-device related to a change in the conduction mechanisms. The higher photogenerated current for b-device indicates that it must result in better performance for solar cell applications.

By considering that these device applications are focused for solar cells, a stability study was conducted to evaluate its feasible degradation under light exposition. For this study, a 360-W incandescent light was used to irradiate the devices with BPhen during 2 and 4 h. The obtained J–V curves after irradiation are shown in **Figure 10**, where **Figure 10A** shows the curves related to the 2-h irradiation and **Figure 10B** to the 4-h irradiation. First, it can be observed that the curve behavior changed compared to the non-irradiated devices (**Figure 9B**). The shape of the curves also changed to an almost linear curve for both devices. For the a-device illuminated curve, smaller current density values than those of the darkness curve are shown, but for b-device, the opposite is observed, showing a more pronounced photo-effect than that of **Figure 9B**, while it is fairly diminished for a-device. Despite this, the current density values for a-device are approximately equal, but for b-device, darkness condition are lower, while illuminated conditions are higher. All of these indicate that complex-a presents a higher stability than complex-b; however, the photo-current density is improved for b-device after a 2-h irradiation. The latter could be related to

various mechanisms related to light interaction and heating of the films. Some of them may change the microstructure and furthermore a crystallization may occur, resulting in a conductivity enhancement, for instance, due to the alignment improvement of the PEDOT:PSS (Kim et al., 2014; Wang et al., 2018; Duan and Uddin, 2020; Kim et al., 2020). Moreover, the J–V curves resulting from the 4-h irradiation are shown in **Figure 10B**, where a noticeable decrease of the current density values, of almost eight orders of magnitude, is observed for the devices compared to the non-irradiated J-V curves. The curve behavior is changed after the irradiation, resembling a diode curve. It is interesting to note that the current density values for both complex device illuminated curves are larger than those for darkness conditions, but the variation is quite small, indicating that the devices were degraded.

The conductivity for the different devices under the previous discussed conditions was calculated and plotted in **Figure 11**. The largest conductivity value (~2.7×10^{-4} S/cm) is observed for the complex-a/BPhen device after 2 h irradiation. The resulting conductivity values are lower than those of the PEDOT:PSS. The conductivity values for each complex device under darkness and illuminated conditions present an enhancement by adding the BPhen film and a further enhancement by the 2-h irradiation process but an abrupt decrease by the 4-h irradiation process (to ~ 10^{-13} S/cm). It is important to note that these effects are more pronounced for a-device under darkness condition but is less pronounced for b-device under darkness condition. The marked electrical behavior change after 4 h irradiation could be related to a degradation of the films and interfaces within the device, limiting the charge carrier mobility and extraction (Duan and Uddin, 2020). A conductivity change of almost 2.1×10^{-4} S/cm was obtained by incorporating the BPhen to a-device, and of almost 1.2×10^{-4} S/cm was obtained by a 2-h irradiation process for b-device under illumination, which are the largest observed effects. Apparently, the chloride radical of complex-b plays an important role on the device conductivity, and also its interaction with the BPhen and device stability.

J–V curves were measured under different light colors for the complex devices with and without the BPhen and are shown in **Figure 12**. **Figure 12A** shows the J–V curves for a-device where a slight change is observed by varying the incident light color and with a non-particular tendency. On the other hand, **Figure 12B** shows the J–V curves for b-device, where a slight change is also observed by varying the incident light color and with a non-particular tendency, but the green light curve values are smaller. For the BPhen devices, **Figures 12C,D** show the J–V curves for a-device and b-device, respectively. **Figure 12C** shows an almost non-observable change by varying the incident light color. However, **Figure 12D** shows a larger curve change by varying the incident light color where the green light color curve presents the largest variation. All of these indicate that b-devices are more susceptible to incident light colors and are more marked for b-complex/BPhen device.

For further analysis for solar cell applications, spectroscopic measurements of external quantum efficiency (EQE) and short-circuit current (JSC) were performed for a- and b-devices at room temperature. **Figure 13A** shows that the wavelength-dependent EQE for both complex devices presents a similar curve shape. For solar cell applications, it is desirable that the EQE curve values were close to 1, and for these devices, an increase of the EQE from 0.6 to 0.8 (400–450 nm) is observed, followed by a slight increase of almost 9–9.5 (450–700 nm) and a slight decrease of 0.8 (700–950 nm), where a more pronounced decrease occurs. However, the EQE curve is higher for b-device, indicating that it presents an enhanced charge carrier generation and collection. The latter could be related to the previous observations in **Figure 13**. In addition, it is interesting to note that the b-device EQE curve presents a decrease to the values of a-device EQE maximum (0.89) at 700 nm. In addition, the higher EQE values lie between 650 and 750 nm. **Figure 13B** allows us to evaluate the wavelength-dependent J_{sc}, where similar curve shapes were obtained for both complexes, but the values are a little higher for b-device, which reaches a maximum of 6.8 mA/cm^2 at 675 nm. It is important to note that the variation is increased in the range from 450 to 650 nm. A sudden decrease of J_{sc} is observed from 6.6 to 4.5 mA/cm^2 and from 700 to 750 nm, which reduces the power output of the device within this range of incident light wavelengths. By comparing to literature where PEDOT:PSS-graphene is used in solar cells and active layers such as perovskites (18–21 mA/cm^2) and other technologies (4.43–14.7 mA/cm^2), the results, respectively, are smaller and lie between the range, but for other PEDOT:PSS-graphene-related technologies (7–36.26 mA/cm^2) the results are close to the lower boundary (Li et al., 2020; Adekoya et al., 2021). All of this indicates that both complex devices present an adequate performance for solar cell applications, where higher conductivities due to a non-chloride radical are presented for complex-a, but a better device conversion efficiency for complex-b is obtained. Nevertheless, further research should be conducted to increase the J_{sc} and improve solar cell performance.

CONCLUSION

Hybrid films of graphene, poly(3,4-ethylenedioxythiophene): poly(styrenesulfonate), and heptacoordinated organotin (IV) complexes were deposited and characterized. The optical properties of hybrid films were investigated via UV–Vis spectroscopy, and the films transmitted more than 70% of light in the wavelength region of 600–1,000 nm, the absorption coefficient is in the order of 10^{-5} cm^{-1} and 10^{-6} cm^{-1}, and the optical band gap is in the range of 2.64 and 3.09 eV. Bathophenanthroline was introduced as the electron transport layer in order to study the solar cell with complete architecture. A conductivity change of up to 2.1×10^{-4} S/cm was obtained by incorporating the bathophenanthroline and almost 1.2×10^{-4}S/cm by a 2-h irradiation process. Conductivity values between 10^{-5} and 10^{-4} S/cm were obtained for the fabricated devices. After irradiation conditions, the electrical behavior of the devices was modified. During the first 2 h, it was improved, but after 4 h, it was degraded. Both complex devices present a good performance for solar cell applications; however, the

morphology of graphene can be an important parameter in the charge transport of these devices.

DATA AVAILABILITY STATEMENT

The raw data supporting the conclusion of this article will be made available by the authors, without undue reservation.

AUTHOR CONTRIBUTIONS

Conceptualization, MESV, RIZS, LH, and EG; Data curation, MESV, LH, IC, and EG; Formal analysis, MESV, LH, IC, and EG; Funding acquisition, MESV and EG; Investigation, RIZS, MESV, LH, and EG; Methodology, RIZS, MESV, LH, IC, EG, and JMGH; Project administration, LH; Resources, LH and EG; Software, MESV and LH; Supervision, MESV; Validation, MV, LH, and IC; Visualization, MESV, LH, RIZS, and JMGH; Writing—original draft, RIZS, MESV, LH, IC, and EG; Writing—review and editing, MESV, RIZS, LH, and EG.

FUNDING

MESV and LH acknowledge the financial support from Anahuac México University, Project numbers NNAIASEVM16070616 and INNDIAHABL170215171. EG thanks PAPIIT (IN206020) for financial assistance.

ACKNOWLEDGMENTS

The authors thank Gerardo Javier Valle Salas for technical support.

REFERENCES

Adekoya, G. J., Sadiku, R. E., and Ray, S. S. (2021). Nanocomposites of PEDOT:PSS with Graphene and its Derivatives for Flexible Electronic Applications: A Review. *Macromol. Mater. Eng.* 306, 2000716. doi:10.1002/mame.202000716

Ahmed, A., El-Hiti, G. A., Hadi, A. G., Ahmed, D. S., Baashen, M. A., Hashim, H., et al. (2021). Photostabilization of Poly(vinyl Chloride) Films Blended with Organotin Complexes of Mefenamic Acid for Outdoor Applications. *Appl. Sci.* 11 (6), 2853. doi:10.3390/app11062853

Akbari, T., Harkinezhad, B., and Hossein-Babaei, F. (2018). P2MM.8 - Conduction Activation Energy in PEDOT:PSS Thin Films. *17th Int. Meet. Chem. Sensors - IMCS* 2018, 840–841. doi:10.5162/IMCS2018/P2MM.8

Al-Muntaser, A. A., El-Nahass, M. M., Oraby, A. H., Meikhail, M. S., and Zeyada, H. M. (2018). Structural and Optical Characterization of Thermally Evaporated Nanocrystalline 5,10,15,20-Tetraphenyl-21h,23h-Porphine Manganese (III) Chloride Thin Films. *Optik* 167, 204–217. doi:10.1016/j.ijleo.2018.04.041

Alharbi, S. R., Darwish, A. A. A., Al Garni, S. E., ElSaeedy, H. I., and Abd El-Rahman, K. F. (2016). Influence of Thickness and Annealing on Linear and Nonlinear Optical Properties of Manganese (III) Chloride Tetraphenyl Porphine (MnTPPCl) Organic Thin Films. *Infrared Phys. Tech.* 78, 77–83. doi:10.1016/j.infrared.2016.07.014

Cantón-Díaz, A. M., Muñoz-Flores, B. M., Moggio, I., Arias, E., De León, A., García-López, M. C., et al. (2018). One-pot Microwave-Assisted Synthesis of Organotin Schiff Bases: an Optical and Electrochemical Study towards Their Effects in Organic Solar Cells. *New J. Chem.* 42 (17), 14586–14596. doi:10.1039/C8NJ02998A

Chen, Q., Zabihi, F., and Eslamian, M. (2016). Improved Functionality of PEDOT:PSS Thin Films via Graphene Doping, Fabricated by Ultrasonic Substrate Vibration-Assisted spray Coating. *Synth. Met.* 222, 309–317. doi:10.1016/j.synthmet.2016.11.009

Cotter, D., Manning, R. J., Blow, K. J., Ellis, A. D., Kelly, A. E., Nesset, D., et al. (1999). Nonlinear Optics for High-Speed Digital Information Processing. *Science* 286, 1523–1528. doi:10.1126/science.286.5444.1523

De Kok, M. M., Buechel, M., Vulto, S. I. E., Van de Weijer, P., Meulenkamp, E. A., De Winter, S. H. P. M., et al. (2004). Modification of PEDOT:PSS as Hole Injection Layer in Polymer LEDs. *Phys. Stat. Sol. (A)* 201, 1342–1359. doi:10.1002/pssa.200404338

Huanli Dong, H., Zhu, H., Meng, Q., Gong, X., and Hu, W. (2012). Organic Photoresponse Materials and Devices. *Chem. Soc. Rev.* 41, 1754–1808. doi:10.1039/c1cs15205j

Dong, X.-C., Xu, H., Wang, X.-W., Huang, Y.-X., Chan-Park, M. B., Zhang, H., et al. (2012). 3D Graphene-Cobalt Oxide Electrode for High-Performance Supercapacitor and Enzymeless Glucose Detection. *ACS Nano* 6, 3206–3213. doi:10.1021/nn300097q

Dong, Y., Chen, C., Zheng, X., Gao, L., Cui, Z., Yang, H., et al. (2012). One-step and High Yield Simultaneous Preparation of Single- and Multi-Layer Graphene Quantum Dots from CX-72 Carbon Black. *J. Mater. Chem.* 22, 8764–8766. doi:10.1039/c2jm30658a

Du, F.-P., Cao, N.-N., Zhang, Y.-F., Fu, P., Wu, Y.-G., Lin, Z.-D., et al. (2018). PEDOT:PSS/graphene Quantum Dots Films with Enhanced Thermoelectric Properties via strong Interfacial Interaction and Phase Separation. *Sci. Rep.* 8, 1–13. doi:10.1038/s41598-018-24632-4

Duan, L., and Uddin, A. (2020). Progress in Stability of Organic Solar Cells. *Adv. Sci.* 7, 1903259. doi:10.1002/advs.201903259

El-Nahass, M. M., El-Deeb, A. F., Metwally, H. S., and Hassanien, A. M. (2011). Influence of Annealing on the Optical Properties of 5,10,15,20-tetraphenyl-21H, 23H-Porphine Iron (III) Chloride Thin Films. *Mater. Chem. Phys.* 125, 247–251. doi:10.1016/j.matchemphys.2010.09.017

El-Nahass, M. M., Ammar, A. H., Farag, A. A. M., Atta, A. A., and El-Zaidia, E. F. M. (2011). Effect of Heat Treatment on Morphological, Structural and Optical Properties of CoMTPP Thin Films. *Solid State. Sci.* 13, 596–600. doi:10.1016/j.solidstatesciences.2010.12.032

Fu, L., Cao, L., Liu, Y., and Zhu, D. (2004). Molecular and Nanoscale Materials and Devices in Electronics. *Adv. Colloid Interf. Sci.* 111, 133–157. doi:10.1016/j.cis.2004.09.004

Ghazi, D., El-Hiti, G., Yousif, E., Ahmed, D., and Alotaibi, M. (2018). The Effect of Ultraviolet Irradiation on the Physicochemical Properties of Poly(vinyl Chloride) Films Containing Organotin(IV) Complexes as Photostabilizers. *Molecules* 23 (2), 254. doi:10.3390/molecules23020254

Gholivand, K., Gholami, A., Schenk, K. J., Esrafili, M. D., and Farshadfar, K. (2015). Supramolecular Assemblies of Organotin(iv)-Diphosphoryl Adducts: Insights from X-Rays and DFT. *RSC Adv.* 5, 98610–98617. doi:10.1039/c5ra15645a

Gueye, M. N., Carella, A., Massonnet, N., Yvenou, E., Brenet, S., Faure-Vincent, J., et al. (2016). Structure and Dopant Engineering in PEDOT Thin Films: Practical Tools for a Dramatic Conductivity Enhancement. *Chem. Mater.* 28 (10), 3462–3468. doi:10.1021/acs.chemmater.6b01035

Günes, S., Neugebauer, H., and Serdar Sariciftci, N. (2007). Conjugated Polymer-Based Organic Solar Cells. *Chem. Rev.* 107, 1324–1338. doi:10.1021/cr050149z

Hains, A. W., Liang, Z., Woodhouse, M. A., and Gregg, B. A. (2010). Molecular Semiconductors in Organic Photovoltaic Cells. *Chem. Rev.* 110, 6689–6735. doi:10.1021/cr9002984

Hilal, M., and Han, J. I. (2018). Improving the Conductivity of PEDOT:PSS to Nearly 1 Million S/m with Graphene on an ITO-Glass Substrate. *Synth. Met.* 245, 276–285. doi:10.1016/j.synthmet.2018.09.011

Jonas, F., and Heywang, G. (1994). Technical Applications for Conductive Polymers. *Electrochimica Acta* 39, 1345–1347. doi:10.1016/0013-4686(94)e0057-7

Kamiya, T., Nomura, K., and Hosono, H. (2009). Electronic Structure of the Amorphous Oxide Semiconductor A-InGaZnO4-X: Tauc-Lorentz Optical

Model and Origins of Subgap States. *Phys. Status Solidi A.* 206, 860–867. doi:10.1002/pssa.200881303

Kepić, D. P., Marković, Z. M., Jovanović, S. P., Peruško, D. B., Budimir, M. D., Holclajtner-Antunović, I. D., et al. (2014). Preparation of PEDOT:PSS Thin Films Doped with Graphene and Graphene Quantum Dots. *Synth. Met.* 198, 150–154. doi:10.1016/j.synthmet.2014.10.017

Kim, G. H., Hwang, D. H., and Woo, S. I. (2012). Thermoelectric Properties of Nanocomposite Thin Films Prepared with Poly(3,4-Ethylenedioxythiophene) Poly(styrenesulfonate) and Graphene. *Phys. Chem. Chem. Phys.* 14, 3530–3536. doi:10.1039/c2cp23517j

Kim, N., Kee, S., Lee, S. H., Lee, B. H., Kahng, Y. H., Jo, Y.-R., et al. (2014). Highly Conductive PEDOT:PSS Nanofibrils Induced by Solution-Processed Crystallization. *Adv. Mater.* 26, 2268–2272. doi:10.1002/adma.201304611

Kim, Y., Kim, Y., and Kim, J. (2020). Highly Conductive PEDOT:PSS Thin Films with Two-Dimensional Lamellar Stacked Multi-Layers. *Nanomaterials* 10, 2211. doi:10.3390/nano10112211

Laidani, N., Bartali, R., Gottardi, G., Anderle, M., and Cheyssac, P. (2008). Optical Absorption Parameters of Amorphous Carbon Films from Forouhi-Bloomer and Tauc-Lorentz Models: a Comparative Study. *J. Phys. Condens. Matter* 20, 015216. doi:10.1088/0953-8984/20/01/015216

Lee, B. H., Lee, J.-H., Kahng, Y. H., Kim, N., Kim, Y. J., Lee, J., et al. (2014). Graphene-Conducting Polymer Hybrid Transparent Electrodes for Efficient Organic Optoelectronic Devices. *Adv. Funct. Mater.* 24, 1847–1856. doi:10.1002/adfm.201302928

Li, W., Cheng, N., Cao, Y., Zhao, Z., Xiao, Z., Zi, W., et al. (2020). Boost the Performance of Inverted Perovskite Solar Cells with PEDOT:PSS/Graphene Quantum Dots Composite Hole Transporting Layer. *Org. Elect.* 78, 105575. doi:10.1016/j.orgel.2019.105575

Ling, Q.-D., Liaw, D.-J., Zhu, C., Chan, D. S.-H., Kang, E.-T., and Neoh, K.-G. (2008). Polymer Electronic Memories: Materials, Devices and Mechanisms. *Prog. Polym. Sci.* 33, 917–978. doi:10.1016/j.progpolymsci.2008.08.001

Lovén, K., Franzén, S. M., Isaxon, C., Messing, M. E., Martinsson, J., Gudmundsson, A., et al. (2021). Emissions and Exposures of Graphene Nanomaterials, Titanium Dioxide Nanofibers, and Nanoparticles during Down-Stream Industrial Handling. *J. Expo. Sci. Environ. Epidemiol.* 31, 736–752. doi:10.1038/s41370-020-0241-3

Luceño Sánchez, J. A., Peña Capilla, R., and Díez-Pascual, A. M. (2018). High-performance PEDOT: PSS/hexamethylene Diisocyanate-Functionalized Graphene Oxide Nanocomposites: Preparation and Properties. *Polymers* 10, 1169. doi:10.3390/polym10101169

Mahmood, Z. N., Yousif, E., Alias, M., El-Hiti, G. A., and Ahmed, D. S. (2020). Synthesis, Characterization, Properties, and Use of New Fusidate Organotin Complexes as Additives to Inhibit Poly(vinyl Chloride) Photodegradation. *J. Polym. Res.* 27, 267. doi:10.1007/s10965-020-02245-8

Makhlouf, M. M., Shehata, M. M., and Abdelhady, K. (2019). Tuning of Structural and Optical Properties of 5,10,15,20-Tetra(4-Pyridyl)-21h,23h-Porphine Thin Films as a Promising Photovoltaic Absorber Material. *Opt. Mater.* 98, 109378. doi:10.1016/j.optmat.2019.109378

Malard, L. M., Pimenta, M. A., Dresselhaus, G., and Dresselhaus, M. S. (2009). Raman Spectroscopy in Graphene. *Phys. Rep.* 473, 51–87. doi:10.1016/j.physrep.2009.02.003

Mansour, A. E., Kim, H., Park, S., Schultz, T., Cao, D. X., Nguyen, T. Q., et al. (2020). Conductive Polymer Work Function Changes Due to Residual Water: Impact of Temperature-Dependent Dielectric Constant. *Adv. Electron. Mater.* 6, 2000408. doi:10.1002/aelm.202000408

Mok, T. M., and O'Leary, S. K. (2007). The Dependence of the Tauc and Cody Optical Gaps Associated with Hydrogenated Amorphous Silicon on the Film Thickness: αl Experimental Limitations and the Impact of Curvature in the Tauc and Cody Plots. *J. Appl. Phys.* 102, 113525. doi:10.1063/1.2817822

Monzón-González, C. R., Sánchez-Vergara, M. E., Vallejo Narváez, W. E., Rocha-Rinza, T., Hernández, M., Gómez, E., et al. (2021). Synthesis and Characterization of Organotin(IV) Semiconductors and Their Applications in Optoelectronics. *J. Phys. Chem. Sol.* 150, 109840. doi:10.1016/j.jpcs.2020.109840

Oh, W.-C., Fatema, K. N., Liu, Y., Jung, C. H., Sagadevan, S., Ud Dowla Biswas, M. R., et al. (2020). Polypyrrole-Bonded Quaternary Semiconductor LiCuMo2O11-Graphene Nanocomposite for a Narrow Band Gap Energy Effect and its Gas-Sensing Performance. *ACS Omega* 5, 17337–17346. doi:10.1021/acsomega.0c01699

Ouyang, J., Chu, C.-W., Chen, F.-C., Xu, Q., and Yang, Y. (2005). High-Conductivity Poly(3,4-ethylenedioxythiophene):Poly(styrene Sulfonate) Film and its Application in Polymer Optoelectronic Devices. *Adv. Funct. Mater.* 15, 203–208. doi:10.1002/adfm.200400016

Pal, U., Samanta, D., Ghorai, S., and Chaudhuri, A. K. (1993). Optical Constants of Vacuum-evaporated Polycrystalline Cadmium Selenide Thin Films. *J. Appl. Phys.* 74, 6368–6374. doi:10.1063/1.355161

Park, C., Yoo, D., Im, S., Kim, S., Cho, W., Ryu, J., et al. (2017). Large-scalable RTCVD Graphene/PEDOT:PSS Hybrid Conductive Film for Application in Transparent and Flexible Thermoelectric Nanogenerators. *R. Soc. Chem. Adv.* 7, 25237–25243. doi:10.1039/c7ra02980b

Pasha, A., Khasim, S., Khan, F. A., and Dhananjaya, N. (2019). Fabrication of Gas Sensor Device Using Poly (3, 4-Ethylenedioxythiophene)-Poly (Styrenesulfonate)-doped Reduced Graphene Oxide Organic Thin Films for Detection of Ammonia Gas at Room Temperature. *Iran Polym. J.* 28, 183–192. doi:10.1007/s13726-019-00689-4

Rattana, T., Chaiyakun, S., Witit-anun, N., Nuntawong, N., Chindaudom, P., Oaew, S., et al. (2012). Preparation and Characterization of Graphene Oxide Nanosheets. *Proced. Eng.* 32, 759–764. doi:10.1016/j.proeng.2012.02.009

Raymo, F. M. (2002). Digital Processing and Communication with Molecular Switches. *Adv. Mater.* 14, 401–414. doi:10.1002/1521-4095(20020318)14:6<401:aid-adma401>3.0.co;2-f

Sajedi-Moghaddam, A., Saievar-Iranizad, E., and Pumera, M. (2017). Two-dimensional Transition Metal Dichalcogenide/conducting Polymer Composites: Synthesis and Applications. *Nanoscale* 9, 8052–8065. doi:10.1039/c7nr02022h

Sánchez Vergara, M. E., Hamui, L., Gómez, E., Chans, G. M., and Galván Hidalgo, J. M. (2021). Design of Promising Heptacoordinated Organotin (IV) Complexes-Pedot:pss-Based Composite for New-Generation Optoelectronic Devices Applications. *Polymers* 13, 1023. doi:10.3390/polym13071023

Sánchez Vergara, M. E., Motomochi-Lozano, J. D., Cosme, I., Hamui, L., Olivares, A. J., Galván-Hidalgo, J. M., et al. (2020). Growth of Films with Seven-Coordinated Diorganotin(IV) Complexes and PEDOT:PSS Structurally Modified for Electronic Applications. *Semicond. Sci. Technol.* 35, 12. doi:10.1088/1361-6641/aba825

Sarkhan, N. A., Rahman, Z. A., Zakaria, A., and Ali, A. M. M. (2019). Enhanced Electrical Properties of Poly(3,4-Ethylenedioxythiophene:poly(4-Styrenesulfonate) Using Graphene Oxide. *Mater. Today Proc.* 17, 484–489. doi:10.1016/j.matpr.2019.06.489

Seol, Y. G., Trung, T. Q., Yoon, O.-J., Sohn, I.-Y., and Lee, N.-E. (2012). Nanocomposites of Reduced Graphene Oxide Nanosheets and Conducting Polymer for Stretchable Transparent Conducting Electrodes. *J. Mater. Chem.* 22, 23759–23766. doi:10.1039/C2JM33949H

Soltani-kordshuli, F., Zabihi, F., Eslamian, M., Zabihi, F., and Eslamian, M. (2016). Graphene-doped PEDOT:PSS Nanocomposite Thin Films Fabricated by Conventional and Substrate Vibration-Assisted spray Coating (SVASC). *Eng. Sci. Technol. Int. J.* 19, 1216–1223. doi:10.1016/j.jestch.2016.02.003

Tsiper, E. V., Soos, Z. G., Gao, W., and Kahn, A. (2002). Electronic Polarization at Surfaces and Thin Films of Organic Molecular Crystals: PTCDA. *Chem. Phys. Lett.* 360, 47–52. doi:10.1016/s0009-2614(02)00774-1

Urbach, F. (1953). The Long-Wavelength Edge of Photographic Sensitivity and of the Electronic Absorption of Solids. *Phys. Rev.* 92, 1324. doi:10.1103/physrev.92.1324

Vidor, F., Meyers, T., and Hilleringmann, U. (2015). Flexible Electronics: Integration Processes for Organic and Inorganic Semiconductor-Based Thin-Film Transistors. *Electronics* 4, 480–506. doi:10.3390/electronics4030480

Wang, X., Zhang, X., Sun, L., Lee, D., Lee, S., Wang, M., et al. (2018). High Electrical Conductivity and Carrier Mobility in oCVD PEDOT Thin Films by Engineered Crystallization and Acid Treatment. *Sci. Adv.* 4, eaat5780. doi:10.1126/sciadv.aat5780

Yang, Y., Ma, L., and Wu, J. (2004). Organic Thin-Film Memory. *MRS Bull.* 29, 833–837. doi:10.1557/mrs2004.237

Yang, Y., Ouyang, J., Ma, L., Tseng, R. J.-H., and Chu, C.-W. (2006). Electrical Switching and Bistability in Organic/Polymeric Thin Films and Memory Devices. *Adv. Funct. Mater.* 16, 1001–1014. doi:10.1002/adfm.200500429

Yeon, C., Kim, G., Lim, J. W., and Yun, S. J. (2017). Highly Conductive PEDOT:PSS Treated by Sodium Dodecyl Sulfate for Stretchable Fabric Heaters. *RSC Adv.* 7, 5888–5897. doi:10.1039/c6ra24749k

Yoo, D., Kim, J., and Kim, J. H. (2014). Direct Synthesis of Highly Conductive Poly(3,4-Ethylenedioxythiophene):poly(4-Styrenesulfonate) (PEDOT:PSS)/graphene Composites and Their Applications in Energy Harvesting Systems. *Nano Res.* 7, 717–730. doi:10.1007/s12274-014-0433-z

Zhang, M., Bai, L., Shang, W., Xie, W., Ma, H., Fu, Y., et al. (2012). Facile Synthesis of Water-Soluble, Highly Fluorescent Graphene Quantum Dots as a Robust Biological Label for Stem Cells. *J. Mater. Chem.* 22, 7461–7467. doi:10.1039/c2jm16835a

Zhokhavets, U., Goldhahn, R., Gobsch, G., and Schliefke, W. (2003). Dielectric Function and One-Dimensional Description of the Absorption of Poly(3-Octylthiophene). *Synth. Met.* 138, 491–495. doi:10.1016/s0379-6779(02)00502-7

Conflict of Interest: The authors declare that the research was conducted in the absence of any commercial or financial relationships that could be construed as a potential conflict of interest.